# Negative Ion Production from Positive Ions Incident in a Metal Vapour

*by*

**GREGORY J. KELLY**

Thesis submitted to the School of Graduate Studies
of the University of Ottawa in partial fulfillment
of the requirements for the degree
of Master of Science in Physics



Physics Department
Faculty of Science
University of Ottawa
Ottawa, Canada
1987

## Abstract

The production of negative ions in charge changing collisions is studied for a positive ion incident in a metal vapour. Negative yields are reported for a positive iodine beam incident in a magnesium vapour. The metal vapour target, which we designed to produce negative ion beams, was adapted to study the charge exchange collisions themselves. Measurements of the double electron capture process, in which two electrons are transfered in a single collision, are reported from 20 keV to 90 keV. A new method is developed to isolate this process from the more highly favoured two step process, where the electrons are transfered in two successive collisions, using the initial growth method. The double electron capture cross section is found to be smaller than expected and does not contribute greatly to the negative equilibrium yields.

## Acknowledgments

I would like to thank Dr. Brian Hird for the confidence and patience he showed and the time he spent with me throughout the past few years.

I would like to thank the entire staff of the physics departement whom it was a pleasure to work with.

I would also like to thank my family and friends who gave me support and encouragement. Finally I would like to express my deep appreciation to Judy Hardwick, who not only gave me close support and encouragement, but also contributed by drawing three of the more involved diagrams.

## Contents

## CHAPTER 1-*Introduction*

Ion beams have been used extensively in many areas of physics to study atoms, molecules, surfaces, and now single crystals. Ion beams also have direct application in areas such as micro- electronics, ion implantation doping, micro-analysis of semiconductors and other processing of surfaces, as well as in the fabrication of electronic components and integrated circuits. Neutralized beams are used in the fusion program to heat and diagnose magnetically confined plasmas.

Using ion-optic methods, well focused and monoenergetic beams can be obtained to probe the structure of the above systems. Ion beams can be obtained over a wide range of energies, from eV to GeV, for a wide range of atomic and molecular ions permitting a systematic study of the different processes involved.

Ion beams are also used to study ions themselves. Many negative ions have been discovered and ionization potentials have been measured using ion beam techniques. Lifetimes of metastable ions have also been established using these methods.

The study of the dynamics of ion-atom collisions themselves are of great importance. For example in plasma physics and laser physics collisions affect the stability and control of the plasma or gas. An understanding of these collisions is essential in the design and operation of any of the aforementioned devices and particularly in the design of ion sources themselves.

Ions extracted from an ion source plasma are positively charged and as a consequence most research has been done with the aid of positive ion beams. Neutral or negative beams allow further study by looking at processes that favour these beams. In order to produce

neutral or negative beams, ions must capture one or more electrons in charge changing collisions. One method of producing neutral or negative beams involves passing a positive ion beam through a metal vapor in which the electron capture cross sections are large.

In the lower keV ion beam energy range the collisions of heavy ions are considered slow. The criterion which is often used is that the incident ion velocity is less than the electron velocity in a classical Bohr orbit. It follows that the interacting system can be described as a quasi-molecule for a short period of time.

The theory of electron transfers in an atomic collision has been extensively investigated, but calculations are difficult. The ion trajectories can be treated classically but the electron configurations must be treated quantum mechanically. Except for some specially simple systems the theory is not yet able to predict the cross sections quantitatively. The theory is particularly difficult for ions of the order 100 keV where neither fast nor slow approximations can be made.

Several processes are possible in an ion-atom collision. Table 1.1 gives a summary of several of these processes for an incident positive ion on a gas target. The relative probability of these different processes will depend on the quasi-molecular structure of the interacting states, and the energy involved in the collision. The energy defect between the quasi-molecular energy levels of the initial and final states is found experimentally to be an important parameter in these collisions. As a general rule, the smaller the energy defect the more a certain process will be favoured. In certain circumstances a choice of ion beams can be made so that a unique, or a few final states are produced; in this way the theoretical interpretations are simplified. Once the structure of the quasi-molecule has

been determined the dynamics of the collisions can be predicted and investigated.

**Table 1.1**

*Summary of processes*

| | |
|---|---|
| $A^+ + B \rightarrow A^{2+} + B + e - \Delta Q$ | electron detachment |
| $A^+ + B \rightarrow A + B^+ - \Delta Q$ | electron capture |
| $A^+ + B \rightarrow A^+ + B^{k+} + ke - \Delta Q$ | ionization |
| $A^+ + B \rightarrow A^+ + B^* - \Delta Q$ | excitation |

This thesis will give a description of ion production, transport and detection, followed by a description of the design and operation of a metal vapour cell. Tests run with an incident iodine beam will also be described.

Magnesium was chosen for the metal vapour for its high negative yields[1] which result partly from its low ionization potentials. Magnesium, which has two loosely bound electrons in its outer shell, has a relatively small second ionization potential leading us to anticipate a large double electron transfer cross section. It is unclear however, whether or not this process has much influence on the thick target yields where the beam components come to equilibrium.

The design of the vapour cell was chosen to optimize the production of large negative ion beams. The design of the cell was based on published descriptions of other such cells, although many modifications were made. Because of interest in the more fundamental collision processes,the cell was adapted to measure charge exchange cross-sections. For an

incident positive ion, in the lower keV energy range, the electron capture process dominates. The incident ion velocity is much higher than that of the target atom in this energy range. The momentum transfer is usually small and therefore the ion is not greatly deviated from its incident path. The cross-sections can be calculated by measuring the charge components of the beam after it has passed through the target. For these measurements a thin target was required so as to reduce the proportion of multiple collisions. A new technique was developed to measure the double electron capture cross-section against a background of two step single captures. A description of this technique along with results obtained for Iodine incident on Magnesium will be presented in this thesis.

## CHAPTER 2-*Ion Production, Transport and Detection*

### 2.1 Ion Sources

Two frequently used ion sources that extract ions from a gas discharge or plasma are the R.F. type (radio frequency) ion source and the arc discharge ion source.

The R.F. type ion source consists of a discharge tube placed in the field of a high frequency oscillator. A low pressure gas, which is fed in through a thermal mechanical leak, fills the discharge tube. Electrons in the gas are accelerated by the oscillating electric and magnetic fields. If the mean free path of electrons is such that sufficient energy is imparted to them by the field to ionize atoms, the discharge will be initiated. The electron flux produced in these collisions must be kept high enough to maintain the discharge and compensate for electrons lost through recombinations and to diffusion. The oscillating field and tube dimensions are matched to allow discharges at gas pressures around $10^{-2}$torr. A positive anode at one end of the tube serves to concentrate the positive ions at the other end near the exit canal. Beyond the canal the positive ions are extracted by a strong electric field. Because of the high mobility of the electrons, the plasma potential is within a few volts of the anode and the positive ions which are accelerated from the plasma boundary to the exit aperture have nearly the full energy corresponding to the anode voltage. The plasma boundary is well defined by the field at this point and can be curved to focus the ions into the canal.

The arc discharge ion source replaces the oscillating field of the R.F. source with a high current filament to maintain the plasma (see Fig. 2.1). This has the effect of reducing the energy spread of ions leaving the source and increases the sources overall efficiency.

Fig. 2.1 Ion Source

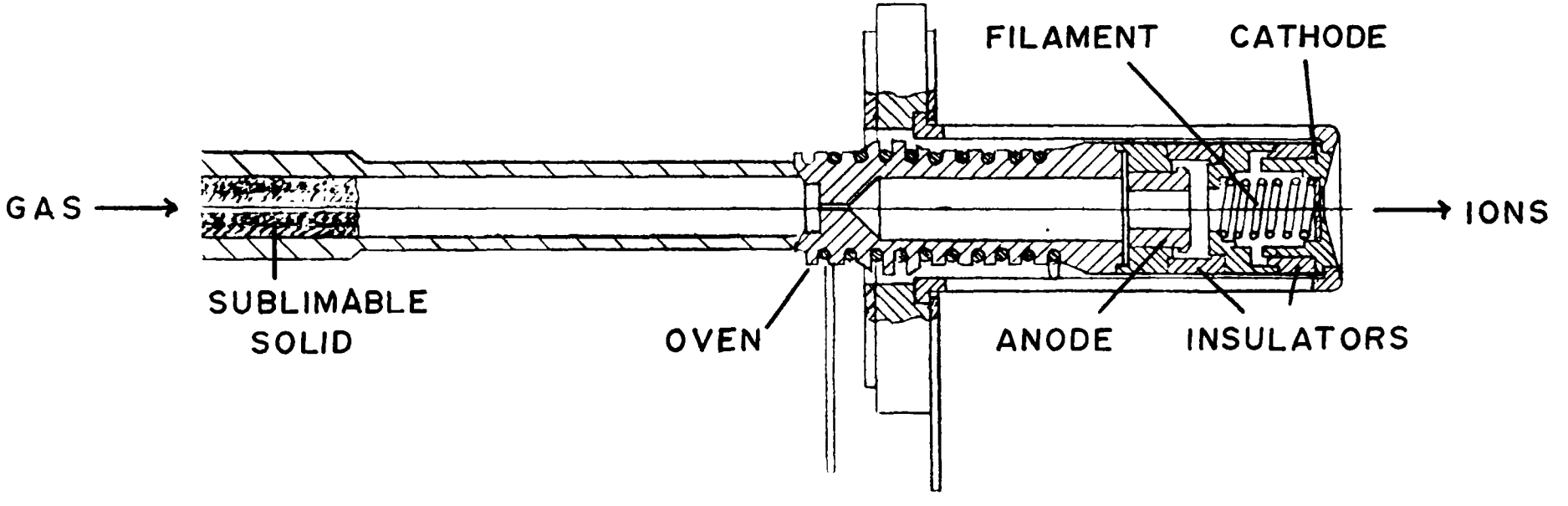

The arc discharge can be very intense over a small volume and is optimized by surrounding it by the filament. This type of source is a hollow cathode source; it produces larger ion beams for a given input power. The arc discharge ion source also has the advantage of generating ions from materials that have low vapour pressures. The model of ion source used in these experiments, the Danfysik 911A, can be used to produce ions from solid materials by heating them in an adjacent oven to increase their vapour pressure. Oven temperatures up to 1700°C can be reached. Any element having a vapour pressure of $10^{-2}$ torr up to this temperature can in principle be used in this source. This covers a large percentage of the elements in the periodic table.

Vapour flows from the oven or gas inlet into the cathode cavity. The cathode consists of an electron emitting filament placed between two electrodes. As the filament heats electrons are thermally emitted from the cathode to ionize the vapour and maintain the discharge. The arc has a negative resistance requiring ballast resistors in the power supply. The arc operates most efficiently at about 50V and gives an arc current of about $10^{-1}$ amps. To initiate the arc a 300V low current supply with an overload short circuit is connected in series with the arc supply. The filament which is in direct contact with the exit aperture keeps the hot vapour from condensing on and blocking the small pin hole aperture. A homogeneous magnetic field is added to the system to counteract the field produced by the helical filament. This is necessary in order to avoid off centre concentrations of the electrons from slightly misaligned magnetic fields.

The following table summarizes the different beams obtained with the Danfysik 911A ions source.

**Table 2.1**
*Ion beams obtained with 911A ion source*

| Element | Vapor temperature at $10^{-2}$torr (K) | Oven-specifications temp. range | current(A) | Beam currents ($10^{-8}$A) |
|---|---|---|---|---|
| Mg | 705 | med. | 20-25 | 1 |
| Na | 560 | med. | 10-20 | 3 |
| Li | 820 | med.-high | 25-30 | 100 |
| I | 260 | - | 0 | 1 |

## 2.2 Ion Transport

Ion beams are formed and transported using electric and magnetic fields. Focussing of the beam is accomplished by the extraction and accelerating fields. The electrode which extracts the ions from the source has the shape of an axial tube. Inside the tube the ions are in a nearly field free region before emerging into the roughly uniform electric field of the accelerator column. The change in axial field between the inside of the extraction electrode and the accelerator creates a radial field (by Gauss's law) which is approximately proportional to the distance off axis. The system thus acts as a focusing lens and it can be shown that the focal length has the following form

$$f \propto \frac{V}{E_2 - E_1}, \tag{2.1}$$

where V is the accelerating voltage, $E_1$ is the small extracting field, and $E_2$ is the accelerating field.

Adjustment of the extraction voltage, which determines $E_2$, provides the main control over the convergence of the beam as it leaves the accelerator. The beam, which initially diverges from the source, becomes slightly convergent after the lens so that it can be focussed at different distances from the accelerator. The 0-10 kV extraction voltage is

adjusted to focus the beam at each of the different energies in the region of the small apertures of the magnesium target.

Ion beams can be directed down long lengths of beamline using magnetic steerers. Steerers consist of coils wound around a square iron core which are placed around the beamline. Coils on opposite sides of the iron square are connected in opposition so that the return field lines must leave the iron core and pass through the beam line. Because only small fields are required to deflect the beam, the iron is far from saturation and has high permeability. Consequently the up/down and left/right fields are substantially independent and the internal field at the beamline is quite uniform.

Bending magnets have the ability to separate out different masses, accomplished by bending each mass at a different radius of curvature. The radius of curvature of an ion in a constant magnetic field is related in a simple way to the momentum, by considering the forces involved:

$$\frac{mv^2}{r} = Bev \qquad 2.2$$

or

$$\frac{P}{r} = Be. \qquad 2.3$$

The momentum dispersion of the magnet follows from Eq. 2.3,

$$\frac{\Delta P}{P} = \frac{\Delta r}{r}. \qquad 2.4$$

Now from equ. 2.2,

$$Br = \frac{mv}{e} \qquad 2.5$$

where

$$v = \left[\frac{2eV}{m}\right]^{1/2}. \qquad 2.6$$

Eliminating $v$ in Eq. 2.5 gives

$$Br = \left[\frac{2mV}{e}\right]^{1/2}. \tag{2.7}$$

For a monoenergetic beam which is accelerated by a fixed potential $V$,

$$\frac{\Delta m}{m} = 2\frac{\Delta r}{r}. \tag{2.8}$$

For example: to separate two masses which differ by 1 a.m.u. at 50 a.m.u. with a magnet radius of 50 cm, the resolving slit $\Delta$r placed at the magnet boundary, must not be larger than 0.5 mm. An energy spread in the beam will also increase the width of the mass spectrum peaks. Rearranging Eq. 2.7 we obtain

$$2m = \frac{eB^2r^2}{V}. \tag{2.9}$$

Using Eq. 2.9 we can identify the different masses by scanning the magnetic field, with everything else constant,

$$m \propto \frac{e^2B^2}{eV} \propto \frac{I^2}{eV},$$

where I is the magnet current, neglecting magnet saturation. Starting from one or two known masses, a plot of ion mass as a function of $\frac{I^2}{eV}$ will identify all other peaks and will serve as a calibration. Here I denotes the magnet current which bends a particular mass m with charge e into the detector at an accelerating voltage $V$. For example, in Fig. 2.2 a mass spectrum was taken with Neon and Krypton gases fed into the ion source. The Neon and Krypton peaks are then the strongest and are easely identified. From the currents which correspond to these two masses other peaks such as Oxygen, Nitrogen and Argon were identified and are plotted in Fig. 2.3. If needed, additional points can be obtained

Fig. 2.2

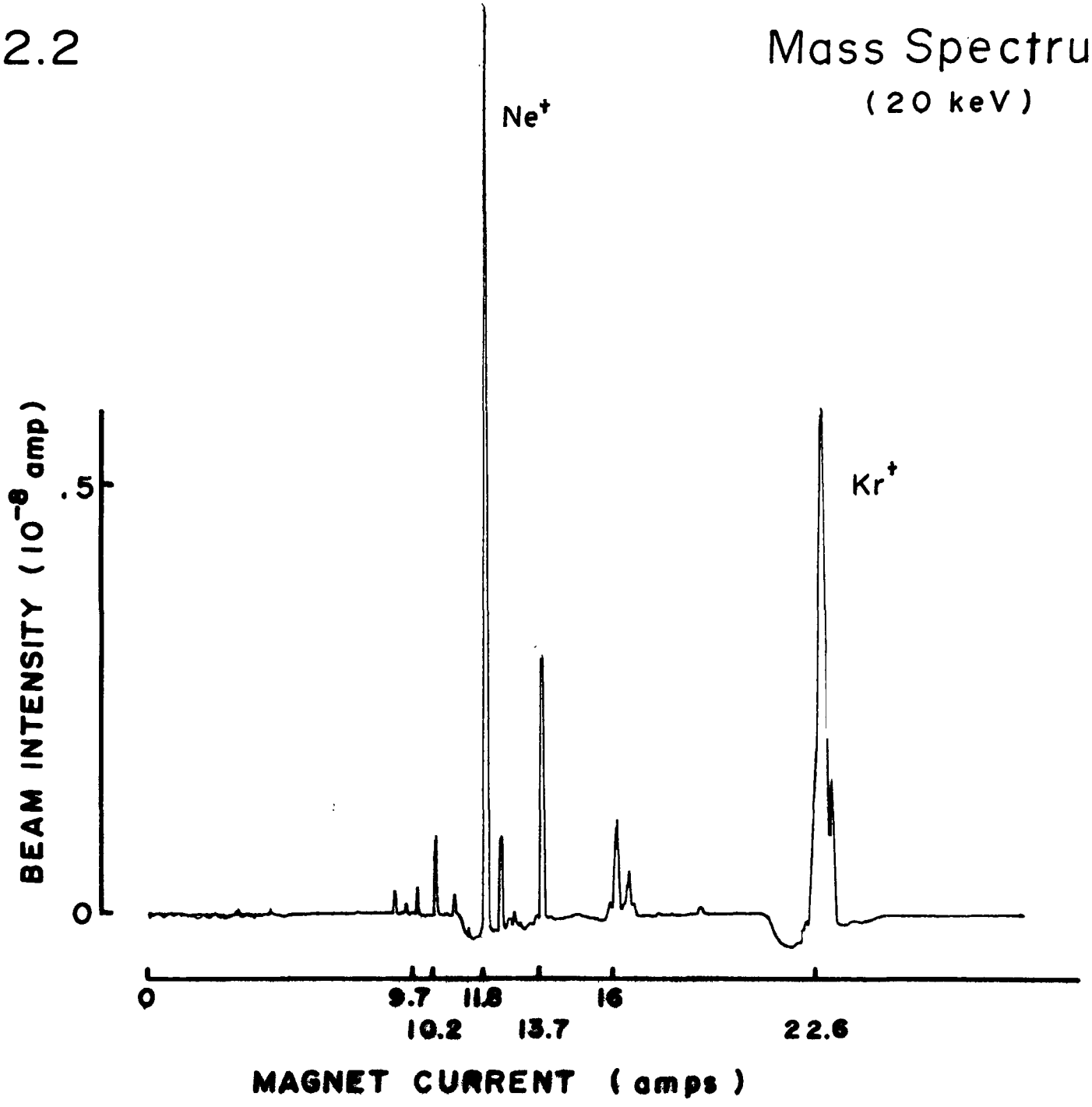
Mass Spectrum
(20 keV)
Ne+
Kr+
BEAM INTENSITY (10⁻⁸ amp)
.5
0
0
9.7
10.2
11.8
13.7
16
22.6
MAGNET CURRENT (amps)

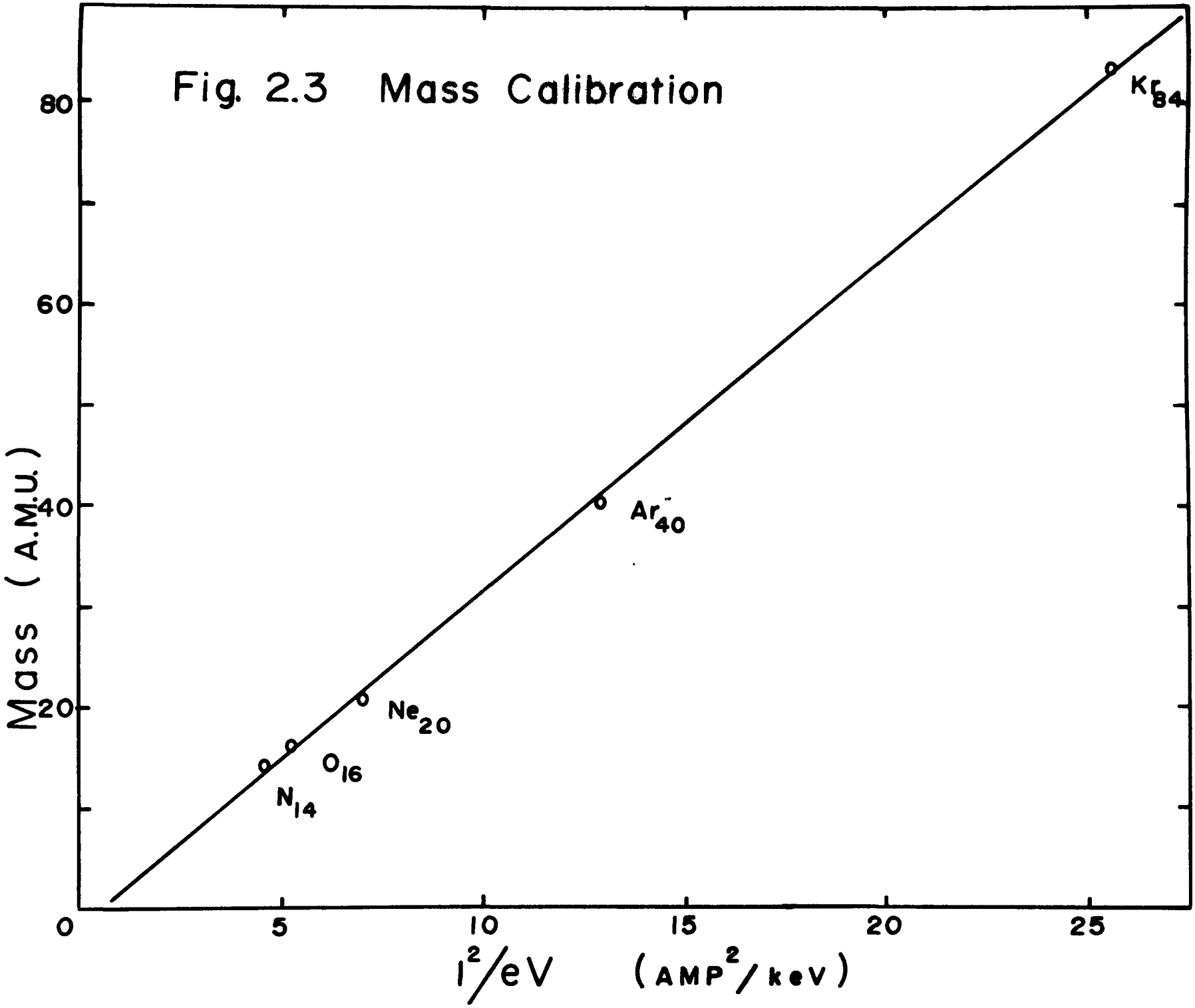
Fig. 2.3 Mass Calibration
Mass (A.M.U.)
80
60
40
20
0
5
10
15
20
25
$I^2/eV$ (AMP$^2$/kev)
$N_{14}$
$O_{16}$
$Ne_{20}$
$Ar_{40}$
$Kr_{84}$

by repeating the procedure for different accelerating velocities or by identifying doubly charged ions, until a unique identification is firmly established.

Bending magnets also have the ability to focus. This ability was not exploited in our experiment since the target was placed before the magnet. The well collimated beam emerging from the target was then bent in a $30^o$ arc into the detection aperture. The aperture was placed directly after the magnet where the beam was still well defined. A 3 mm slit was found sufficient to separate out all peaks.

### 2.3 Ion Detection

Ions can be detected by measuring current flowing in or out of a metal surface or cup, placed in the path of the beam. Ions incident on a metal surface are absorbed in the surface, however secondary electrons can be emitted from the surface. Secondary emission can be as high as 10 electrons per incident ion[2] depending on the type of ion and surface conditions and must be taken into account when attempting to measure absolute currents. In order to get an absolute measure of the current, secondary emission must be suppressed. This is accomplished using a Faraday cup system (see Fig. 2.4). Here a 40 cm long suppression tube and a negative voltage of 200 volts on the aperture returns secondary electrons back to the cup. Only the high energy positive ions can pass the potential barrier and the current measured is then that of the ions entering the cup only.

To assure beam purity the following procedure was followed. After a specific mass was identified, the source was flushed with that element and the system was run for a sufficient length of time such that any extraneous peaks disappeared. A complete scan of the masses was repeated until beam purity was assured, particularly in the region of the mass being

was repeated until beam purity was assured, particularly in the region of the mass being studied. The resolving slits were then replaced by larger apertures to assure capture of the complete beam. Apertures were chosen large enough to capture ions scattered at angles up to $2^o$ in target collisions.

Variation of the separating magnet current permitted a scan of the geometry of the beam profile as it entered the Faraday cup (see Fig. 2.5). This showed a plateau in all cases indicating good detection efficiency across the cup. However, at high beam currents a negative background current was detected and attributed to slit scattering. This was most evident when the beam was not accurately optimized. The sharp edge of the plateaus establishes that the small angle scattering, due to the charge changing collisions, is small compared to the angle of acceptance of the Faraday cup. The magnet and vacuum system were symmetric about the incident ion beam. The positive and negative ions, which have equal and opposite deflections in the magnet, emerged through different exits and were simultaneously measured in two similar Faraday cups (see Fig. 3.5). Currents were measured by two Keithley picoammeters. Stable beams were compared on both sides by changing magnet polarity. This showed agreement within 3% for both positive and negative beams for a wide range of beam intensities.

Fig. 2.4 Faraday Cup

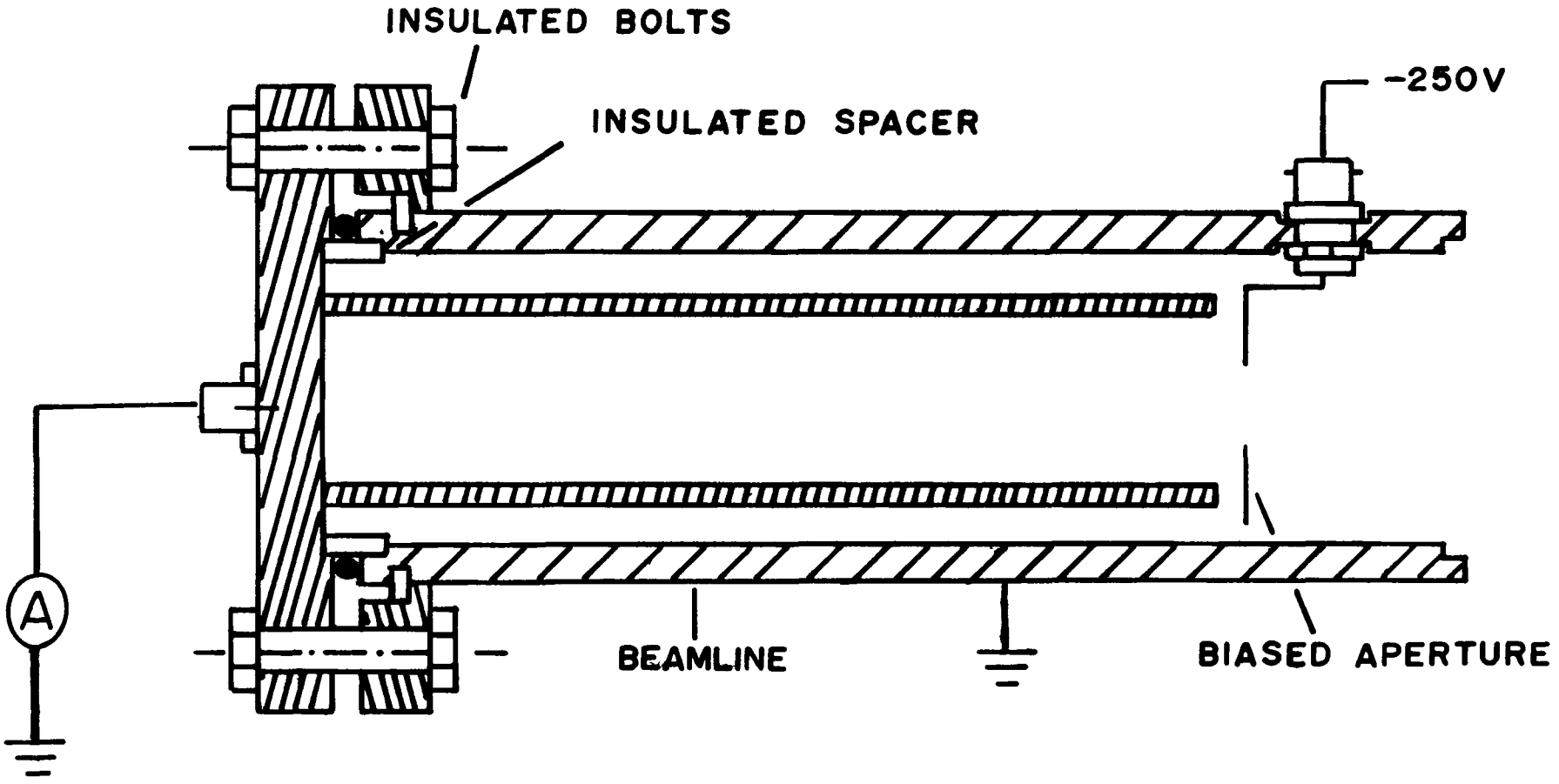

Fig. 2.5 Mass Spectrum ( ENLARGED APERTURES ), 50keV

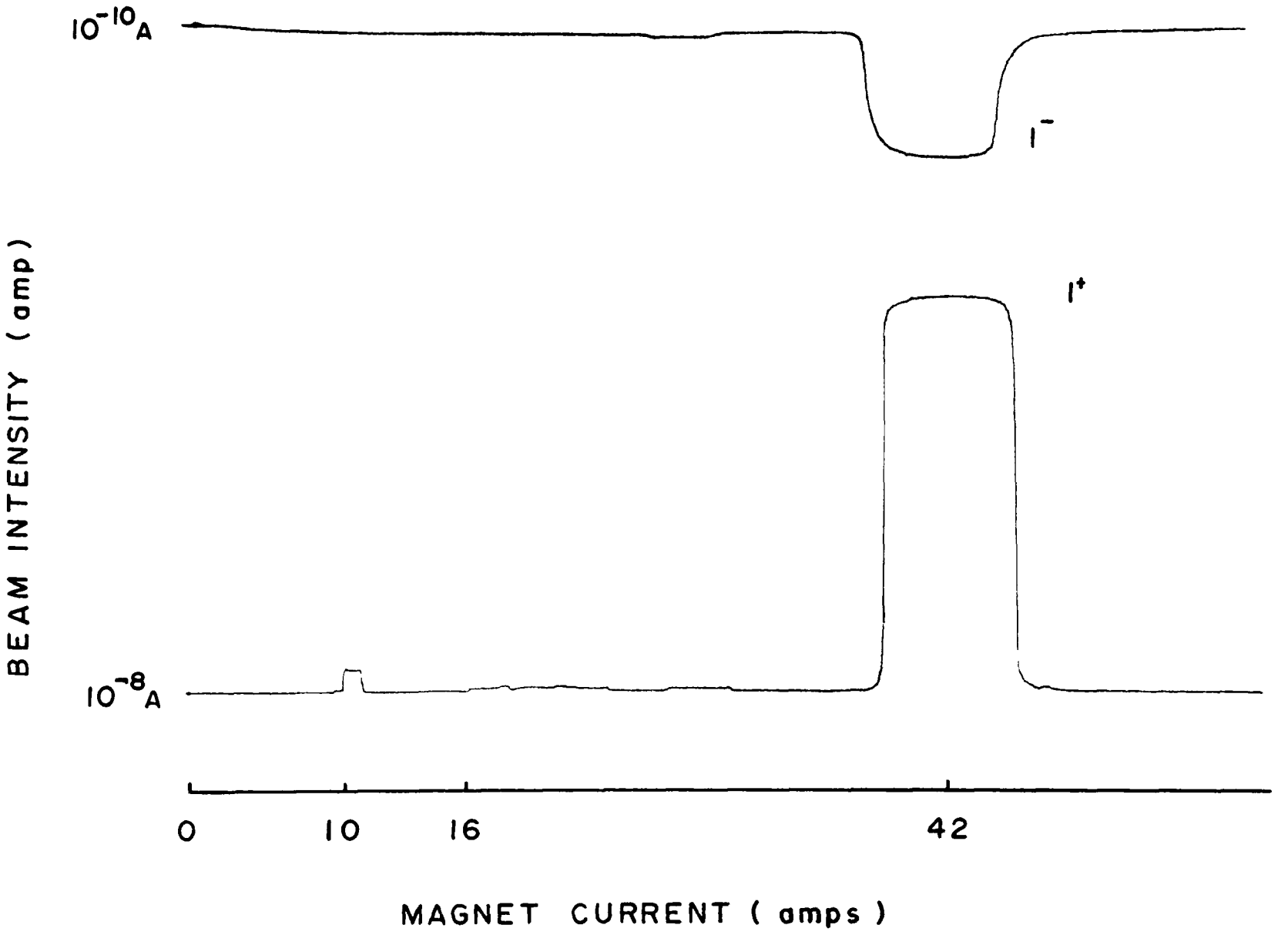

# CHAPTER 3- *Negative Ion Production*

## 3.1 Mechanical Details

The target was machined from a stainless steel cylinder 4" long and 2" in diameter. A passage $\frac{1}{2}$" in diameter was drilled through the center along the axis of the cylinder. The ends were enlarged to $\frac{3}{4}$" and threaded so as to locate entrance and exit slits (see Fig. 3.1). Additional holes, parallel to the axis and surrounding the central cavity, held ceramic rods containing the heating wire. Two remaining holes were used for the thermocouples which controlled the target temperature. The reservoir containing magnesium was connected to the bottom of the cylinder using a standard mini conflat coupling. A $\frac{1}{4}$" hole linked the reservoir and target cavities.

## 3.2 Power Requirements

The target was required to operate at temperatures up to 500°C depending on the vapour pressure of the sublimating metal and had to be stabilized to within 1°C. Elementary calculations showed, neglecting heat loss by conduction, the radiation loss for a cylinder of this size at this temperature would exceed 80W if it were surrounded by one radiation shield, but the heating power could be reduced to about 45W if double radiation shields were used. The reduced temperature from the double radiation shield would also reduce the stress on glass metal seals used for electrical feed-through into the vacuum and O-rings around the target. To reduce the temperature of the surrounding O-rings even further, holes were drilled in the targets support flange and water cooling was added. In order to reduce losses through thermal conductivity the target was supported by ceramic

Fig. 3.1 Target (side)

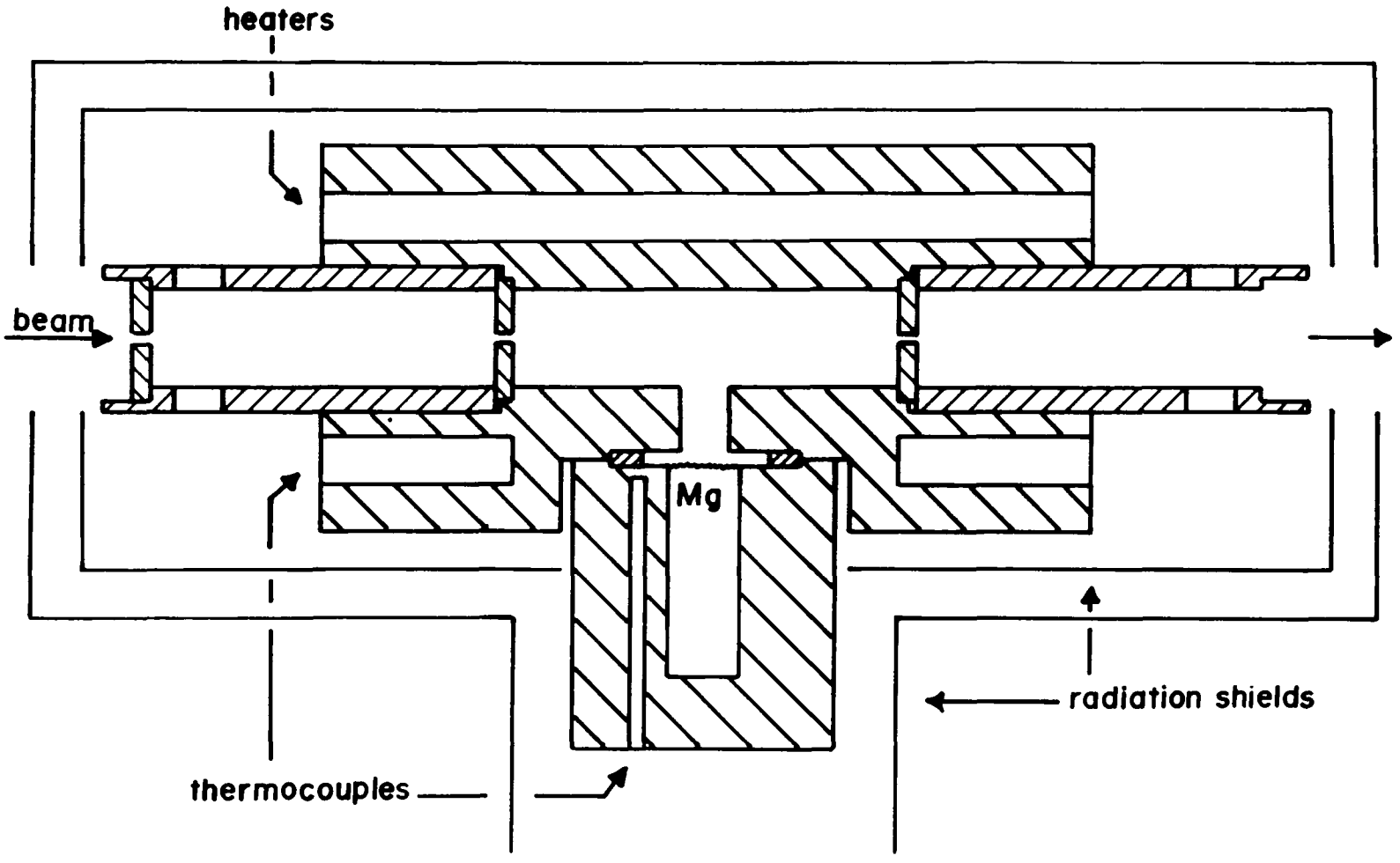

dowels placed between the target and each of the radiation shields, and finally the complete assembly was supported on two v-blocks (see Fig. 3.2). This system also assured a uniform temperature across the target.

The heating was provided by nichrome wire #27AWG. Several tests showed that higher AWG numbered wire failed when heated over long periods of time. Care was also taken when testing not to exceed the current limitations of the heating power supply and circuit. A double length of wire was threaded through five ceramic rods which were then pushed into holes surrounding the target cavity. The wire had a resistance of 10 ohms and required about 25VAC., which was supplied through a variac and a step-down transformer (see Fig. 3.3). The heater was found to easily raise the temperature of the target to 450°C in about two hours.

Some difficulty was encountered in stabilizing the target's temperature. A solid state relay, placed between the temperature controller and the variac, served to switch the power on and off. The controller's thermostat, which was operated by the thermocouple placed in the target, contained integration and differentiation time constants which responded to the rate of temperature change and its previous values. This information was used by the controller to switch the relay in such a way that the temperature oscillations were damped out in a minimum amount of time. The integration and differential time constant adjustments on the controller however could not compensate for the long time constant of the well shielded target. Capacitors in the feed-back circuits were increased by a factor of 10, the temperature then stabilized within 15 minutes of reaching the desired value, and then remained stable within the $1^{o}$ digital temperature readout.

Fig. 3.2 Target (front)

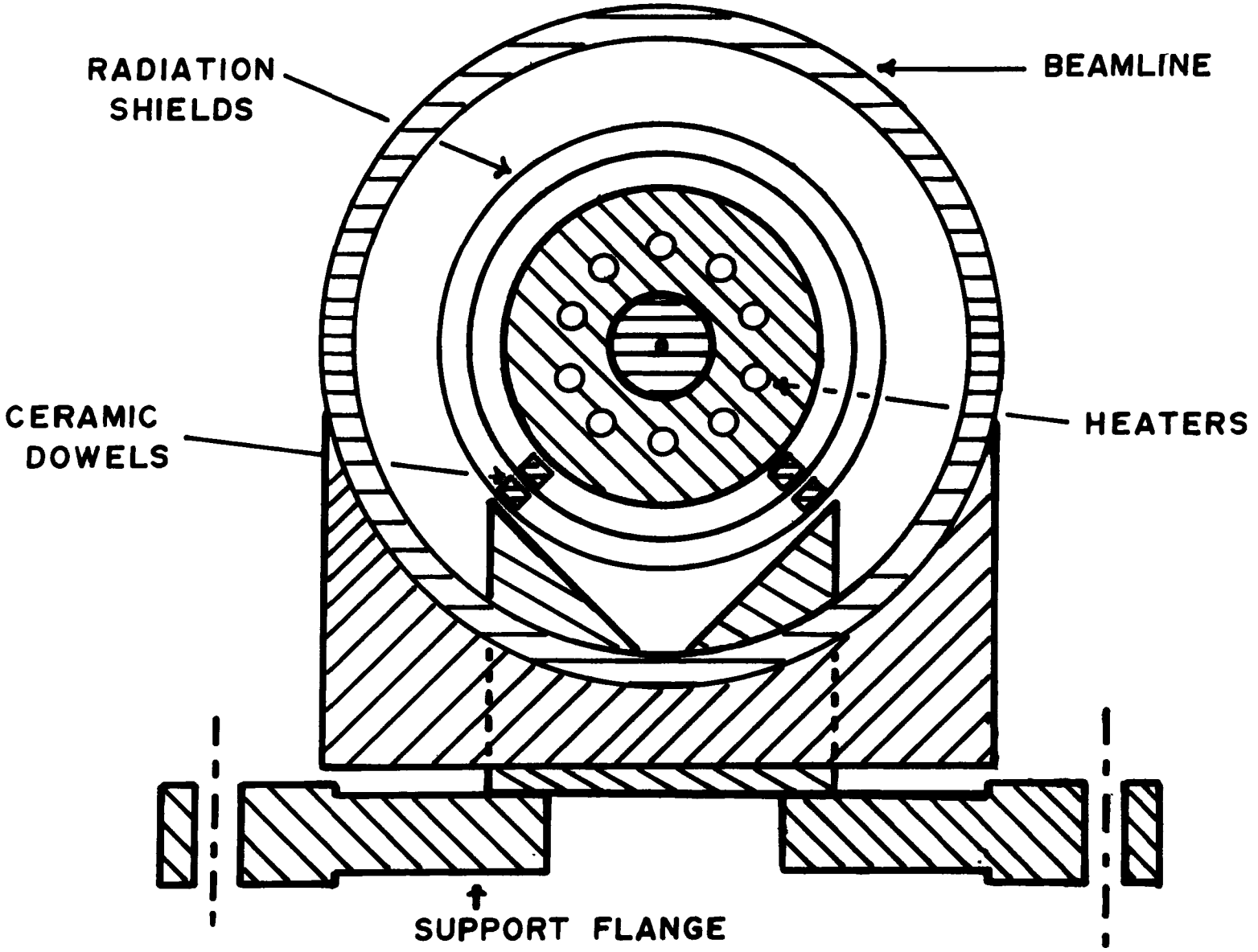

Fig. 3.3 Heating Circuit

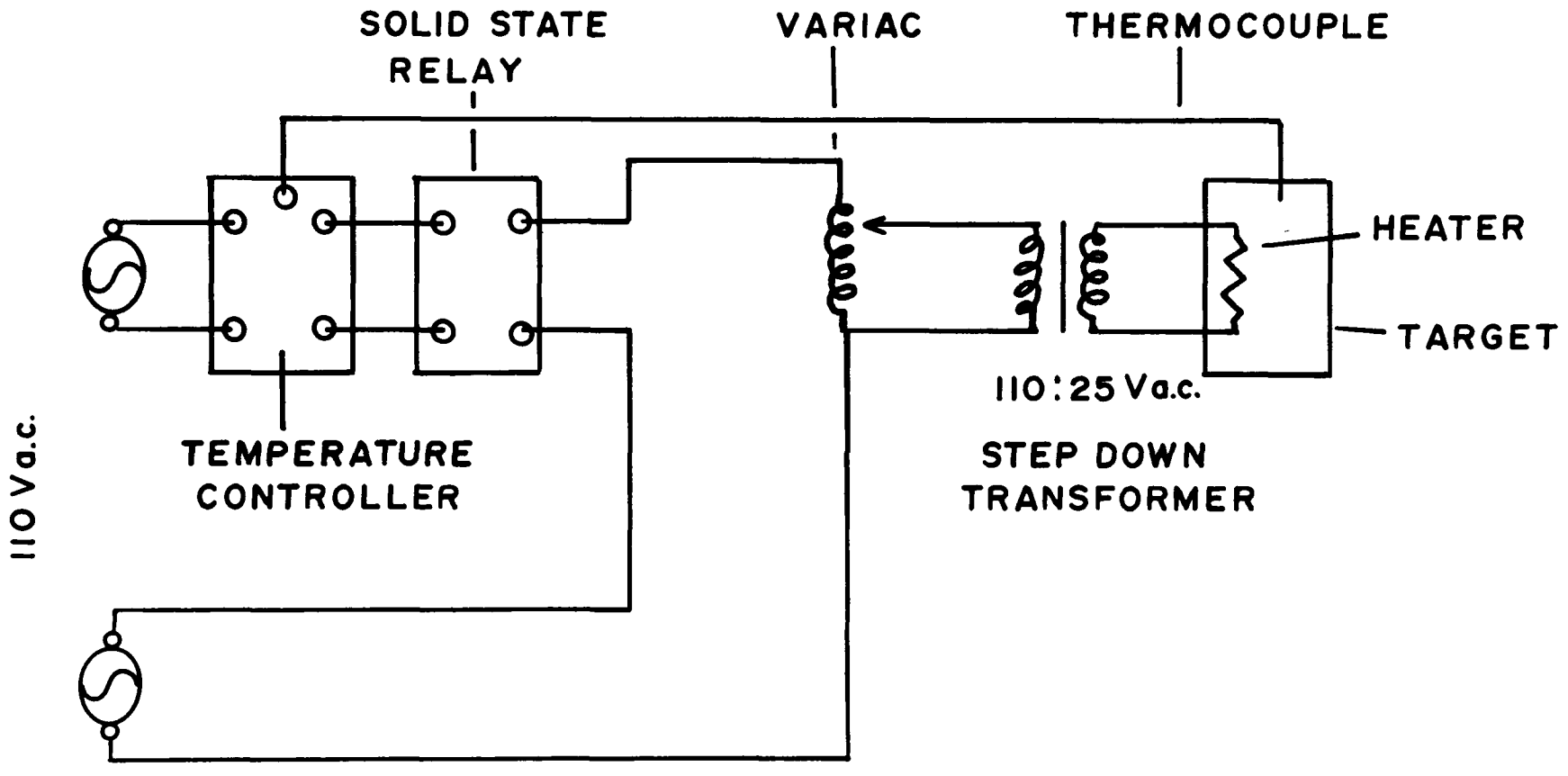

### 3.3 Reservoir

The reservoir, which was suspended radially from the center of the target cylinder, was also machined from stainless steel cylinder $1\frac{1}{2}$" high and $1\frac{1}{3}$" in diameter. Three thermocouple holes were bored parallel to the inner cavity to measure the temperature near the sublimating surface.

In order to keep vapour from condensing on the entrance and exit slits, the reservoir temperature had to be kept below that of the target. Initially the reservoir was heated separately and was thermally isolated from the target by a thin walled tube (see Fig. 3.4). The target could be preheated to over 400°C without lifting the reservoir temperature over 50°C. The purpose of this was to keep the target hot for long periods of time without depleting the magnesium reservoir, which could then be quickly brought to temperature when required.

A flange was placed between the thin walled tube and the reservoir to hold the heating coil. An attempt was made to make coils using LSD moldable paste and nichrome heating wire. A first layer of paste was applied to a metal rod. After drying, the heating wire was then coiled around the molded tube and covered with a second layer of paste. The coil was then removed from the metal rod and placed around the reservoir heating flange. Coils made in this way were successfully used to heat the reservoir but were found difficult to outgas under vacuum. Finally ceramic beads were used to cover the heating wire which was then coiled around the heating flange.

After initial tests, where the target was successfully heated and stabilized, the system was disassembled. Magnesium was found to deposit along the thin walled tube which

Fig. 3.4 Reservoir

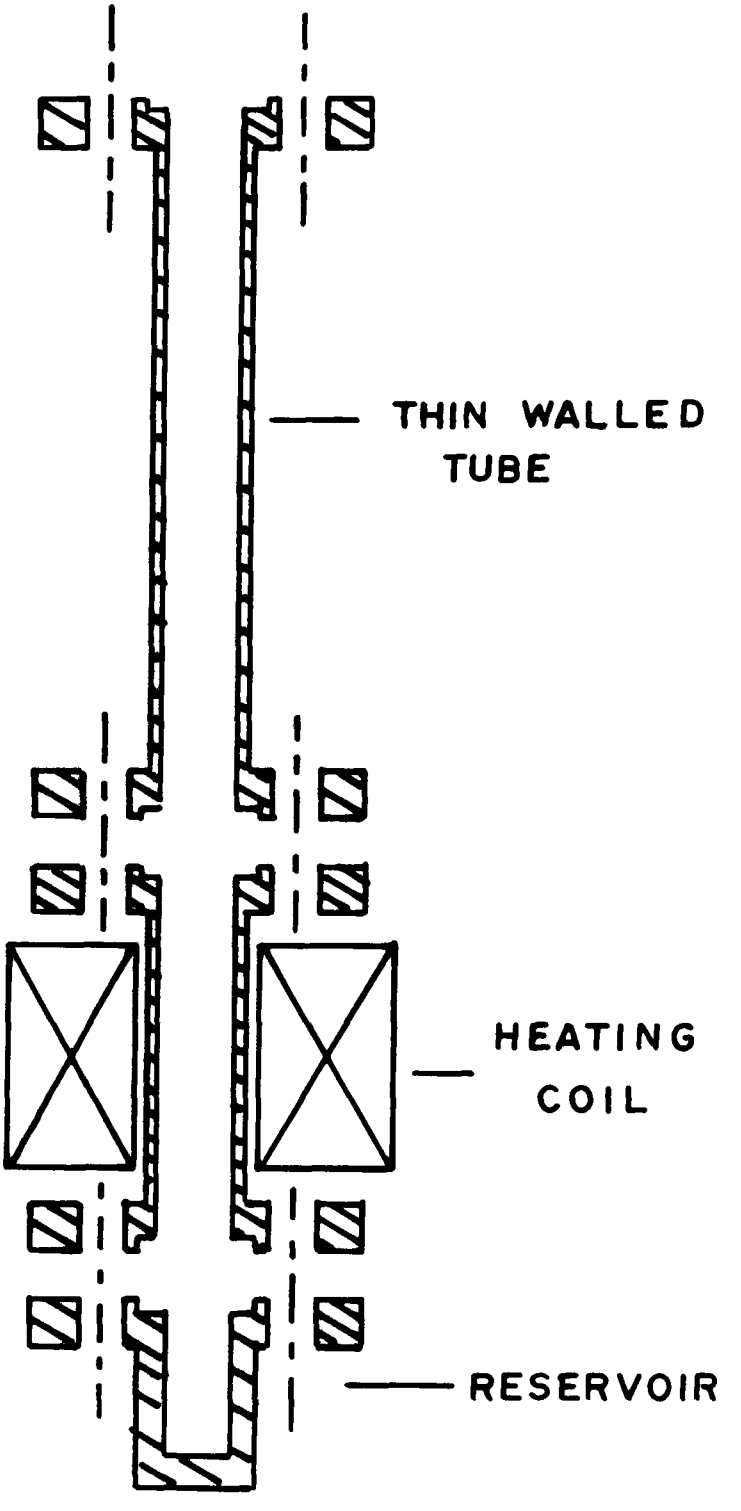

eventually clogged. This indicated that colder regions existed along the tube than in the reservoir itself. Magnesium was also found to deposit around the entrance and exit apertures but did not clog the holes themselves. This design was abandoned and improved versions were tried with the tube diameter increased and insulation added around the tube. These designs were successful in producing high magnesium vapour pressures appropriate for negative ion beam production. For cross section measurements however, reservoir temperatures are more critical in order to evaluate the vapour pressure. In this case the reservoir was bolted directly to the target and heated by downward conduction only. With only one radiation shield surrounding the reservoir its temperature could still be maintained below that of the target. The target would then have to be kept below 200°C overnight but could still reach maximum temperatures in less than two hours.

### 3.4 Experimental Set Up

The target was installed and optically aligned between the accelerator and a 30° deflection charge-separating magnet (see Fig. 3.5). Two steering magnets were positioned before the target to accurately direct the beam both in position and direction, through the target. The target was mounted inside a 4" diameter vacuum tube. Two flexible bellows on either side of the target permitted some manipulation of the target position; the target could also be pre-adjusted using the locating screws which supported the target cylinder inside the vacuum. After optical alignment the position of the target was optimized to give maximum beam current.

The beamline was pumped by two diffusion pumps, one placed near the accelerator and the other near the target itself. A single rotary pump was used to back both diffusion

Fig. 3.5 Apparatus

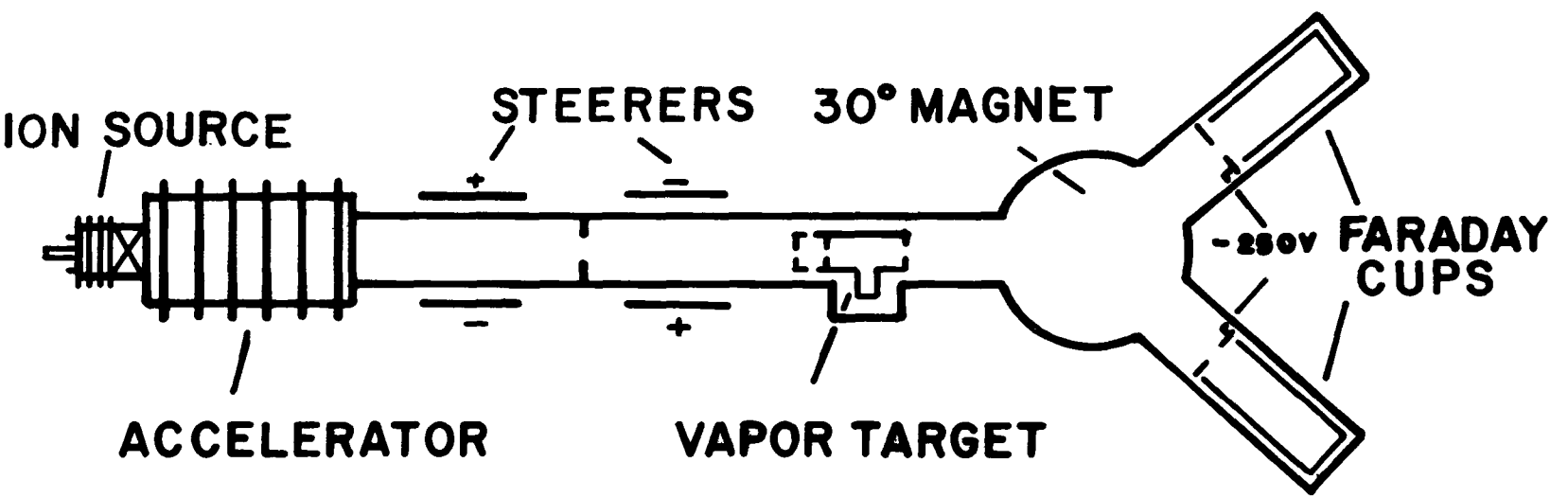

pumps. A gate valve was added in the beamline between the target and accelerator so that the outgassed target was not exposed to air when the ion source was replenished or the filament replaced.

The negative conversion yield of a particular positive ion incident on the vapour target depends on the cross sections for charge changing collisions. If these cross sections are known, the yields can be calculated. Experimentally it is easier to determine the conversion yields than the cross sections, particularly the equilibrium values which occur for thick targets. This method will be described in the following section.

### 3.5 Differential Equations

When a beam of one particular charge traverses a gas target it will emerge composed of several charged components. The relative intensity of each component will depend on the cross sections involved and the target thickness $\pi$ (given in atoms/unit area). The target thickness is related to the target pressure p, temperature t, and length L in the following way

$$\pi = \frac{NpL}{Rt} \tag{3.1}$$

where N and R are Avogadro's number and the gas constant.

Multiplying a given cross section by the target thickness gives the probability for that process to occur. As the target thickness increases the variation in size of the different charged components may be expressed by the following equations (neglecting doubly charged ions):

$$\frac{dF_-}{d\pi} = -F_-(\sigma_{-0} + \sigma_{-+}) + F_0\sigma_{0-} + F_+\sigma_{+-} \tag{3.2}$$

$$\frac{dF_0}{d\pi} = -F_0(\sigma_{0+} + \sigma_{0-}) + F_-\sigma_{-0} + F_+\sigma_{+0} \tag{3.3}$$

$$\frac{dF_+}{d\pi} = -F_+(\sigma_{+0} + \sigma_{+-}) + F_-\sigma_{-+} + F_0\sigma_{0-} \qquad 3.4$$

where $F_i$ is the fraction of ions in charge state i = -, 0, + and $\sigma_{ij}$ is the cross section for a transition from state i to state j. These three linearly dependant equations can be separated and solved.

### 3.6 Charge Fractions

For sufficiently thick targets, the beam current fractions come to an equilibrium, which is independent of the target thickness. If these processes can be described by a two or three component system[3], i.e. doubly charged ions are neglected, the solutions to equations 3.2, 3.3 and 3.4 become relatively simple. The equilibrium charge fractions can be obtained by setting the derivatives to zero. Assuming all projectiles are in one of the three states the following expression holds

$$F_+ = 1 - (F_0 + F_-). \qquad 3.5$$

Inserting Eq. 3.5 into 3.2 and 3.3,

$$-F_{-\infty}a + F_{0\infty}b + \sigma_{+-} = 0 \qquad 3.6$$

$$-F_{0\infty}c + F_{-\infty}d + \sigma_{+0} = 0 \qquad 3.7$$

where

$$a = \sigma_{-0} + \sigma_{-+} + \sigma_{+-} \qquad 3.8$$

$$b = \sigma_{0-} - \sigma_{+-}$$

$$c = \sigma_{0+} + \sigma_{0-} + \sigma_{+0}$$

$$d = \sigma_{-0} - \sigma_{+0}$$

solving equations 3.6 and 3.7 for $F_{-\infty}$ and $F_{0\infty}$,

$$F_{-\infty} = \frac{\sigma_{+0}b + \sigma_{+-}c}{e} \tag{3.9}$$

$$F_{0\infty} = \frac{\sigma_{+-}d + \sigma_{+0}a}{e} \tag{3.10}$$

where

$$e = ac - db.$$

The final charged fractions are just a combination of the different competing processes. Inserting Eq. 3.8 into 3.9, 3.10, and 3.5,

$$F_{-\infty} = \frac{(\sigma_{0-} + \sigma_{0+})\sigma_{+-} + \sigma_{+0}\sigma_{0-}}{e} \tag{3.11}$$

$$F_{0\infty} = \frac{(\sigma_{-0} + \sigma_{-+})\sigma_{+0} + \sigma_{-0}\sigma_{+-}}{e} \tag{3.12}$$

$$F_{+\infty} = \frac{(\sigma_{0+} + \sigma_{0-})\sigma_{-+} + \sigma_{0+}\sigma_{-0}}{e}. \tag{3.13}$$

Heinemeier et al.[1,4,5] found in general that the negative equilibrium yields $F_{-\infty}$, increased with targets having low ionization potentials, and with projectiles having high electron affinities. Exceptions were found however in cases where projectiles with large electron affinities such as $O^+$ and $Cl^+$ were incident on magnesium. In these cases the equilibrium yields were higher than those in the alkali metal vapours such as Na and Li even though these elements have lower ionization potentials.

Magnesium was chosen as the metal vapour for its high negative yields for ions with high electron affinities. Alkali metals such as sodium, lithium and cesium give higher yields for ions with lower electron affinities but require higher sublimation temperatures. A more elaborate target system would also be needed in these cases to confine vapour to the cell

and to avoid contamination inside the beamline. A positive iodine beam was used to test the target. Iodine which has a relatively high electron affinity (3.1 eV) is known to give negative yields of up to 90% in our energy range[1].

### 3.7 Test Run To Produce Negative Ion Beam

Positive iodine ions were extracted and accelerated to energies ranging from 10 to 100 keV, after passing through the magnesium vapour the two charged components of the beam were separated then detected by two Faraday cups.

For negative ion production, slits were chosen to accept a maximum of the beam profile. Kinetic theory shows however that under molecular flow conditions, mass flow through an aperture is proportional to the square of its radius; if the slits are replaced by tubes of length L the mass flow is reduced by a factor of[6]

$$\frac{1}{1+\frac{3L}{8r}} \qquad 3.14$$

where r is the radius of the tube. This enables the acceptance of the target to be increased without increased vapour loss. Tubes $1\frac{1}{2}$" long and $\frac{1}{16}$" internal diameter were installed. Iodine beams of up to $10^{-8}$ amps were obtained through the target with this geometry. The magnesium vapour showed no effect on beamline pressures; pressures stayed below $10^{-6}$ torr after the target was initially outgassed.

After outgassing the target at high temperature for several hours the target was stabilized at 470°C. Relative charge fractions were measured from this temperature down to a temperature of 390°C where the negative component was about 1% (see Fig. 3.6). The negative current reached a maximum at about 440°C where beam diffusion began to

decrease the currents. At this point the negative yield was larger than that of the positive but the beam had been greatly quenched.

At our highest target thickness the positive fraction was still decreasing towards a small fraction, in agreement with the results of Heinemeier et al. where the positive fraction was only a few percent of the beam in equilibrium. The neutrals were not measured in our experiment but the initial rise of negatives and decrease of positives with increasing target thickness was quantitatively similar to curves published by Heinemeier et al., for projectiles with high electron affinities. Table 3.1 summarizes the negative ion beams obtained with the magnesium target.

**Table 3.1**
*Negative ions produced in magnesium vapour*

| Element | Electron Affinity (eV) | Positive Beam ($10^{-8}$A) | Negative Beam ($10^{-10}$A) | Conversion Efficiency $390^{o}C$ (%) | $420^{o}C$ (%) |
|---|---|---|---|---|---|
| Mg | - | 1 | - | - | - |
| Na | 0.546 | 1 | .12 | .12 | - |
| Li | 0.620 | 28 | 1.5 | .05 | - |
| I | 3.061 | 1 | 1.3 | 1.3 | 25 |

Magnesium, which has a higher first ionization potential than the alkali metals, has a lower second ionization potential, leading us to anticipate a large double electron capture cross section. As stated earlier it is unclear whether or not this process has much influence on the negative yields. On the other hand if,

$$\sigma_{+-} << \sigma_{+0}$$

Fig. 3.6 Negative Yields

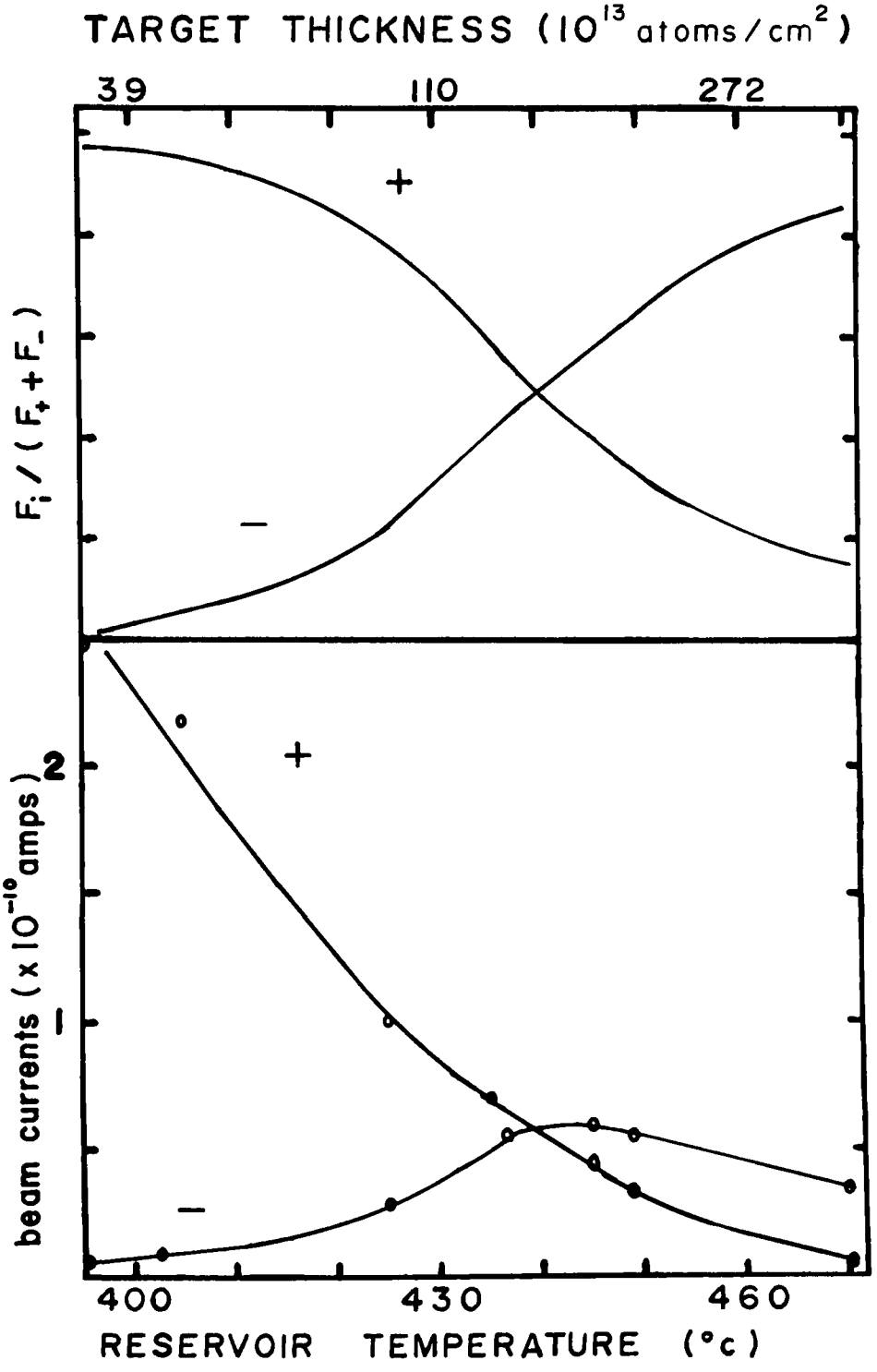

then from equations 3.11 and 3.12,

$$\frac{F_{-\infty}}{F_{0\infty}} = \frac{\sigma_{0-}}{\sigma_{-0}}. \qquad 3.15$$

Heinemeier et al.[1] used this relation to compare experiment with theory. Since $\sigma_{-o}$ varies slowly in this energy range, they found that $F_{-\infty}$ reflects the predicted maximums in the $\sigma_{o-}$ cross sections. They also extracted the individual capture and loss cross sections using a least square fit to the full growth curves. The double electron capture cross section was poorly determined by this method however and it was difficult to estimate the limitations of the approximation used by Heinemeier et al. which entirely neglected this cross section. In equilibrium the target is considered infinitely thick so that each incident ion makes enough collisions for the beam components to come to equilibrium. In equilibrium, many different types of charge transfer collisions contribute, though single electron capture and detachment probably dominate. In order to study double electron capture, the lower temperature, thin target region of Fig. 3.6 would have to be explored, where this cross section is not masked by the two step single electron captures. In the following chapter a more accurate method to measure the double electron capture cross section using the initial growth method will be described and applied.

## CHAPTER 4- *Cross Sections*

### 4.1 Initial Growth Method

The initial growth method is applicable under thin target conditions only. Under thin target conditions, only a small fraction of the ions make collisions and consequently very few of these make a second collision. Under these conditions $N^j$ or $F^j$ in equations 3.1, 3.2 and 3.3 can be expanded in a power series and a more general solution can be obtained (j = -1, 1, 0 now represents the singly charged and neutral components). The three differential equations can be represented by the following equation,

$$\frac{dN^j}{d\pi} = \sum_{i \neq j} \left[\sigma_{ij} N^i - \sigma_{ji} N^j\right] \tag{4.1}$$

where $N^i$, $N^j$ are the number of ions in charge state i and j respectively. Let

$$\sigma_{ii} = -\sum_{i \neq j} \sigma_{ji} \tag{4.2}$$

then Eq. 4.1 becomes

$$\frac{dN^j}{d\pi} = \sum_i \sigma_{ij} N^i. \tag{4.3}$$

The series solution has the following form[7],

$$N^j = N_0^i \left[\delta_{ij} + \sigma_{ij}\pi + \frac{1}{2}\sum_n \sigma_{in}\sigma_{nj}\pi^2 + \ldots\right]. \tag{4.4}$$

For an incoming positive beam we let i = +1, and for the negative component we let j = -1. Eq. 4.3 then becomes (to second order in $\pi$):

$$N^- = N_0^+[\sigma_{+-}\pi + \frac{1}{2}(\sigma_{++}\sigma_{+-} + \sigma_{+0}\sigma_{0-} + \sigma_{+-}\sigma_{--})\pi^2]. \tag{4.5}$$

From Eq. 4.2

$$\sigma_{++} = -(\sigma_{+0} + \sigma_{+-})$$

$$\sigma_{--} = -(\sigma_{-0} + \sigma_{-+}). \qquad 4.6$$

Inserting Eq. 4.6 into 4.5

$$N^- = N_0^+ \sigma_{+-} \pi \left[ 1 - \frac{1}{2}(\sigma_{+0} + \sigma_{+-} + \sigma_{-0} + \sigma_{-+} + \frac{\sigma_{+0}\sigma_{0-}}{\sigma_{+-}})\pi \right]. \qquad 4.7$$

For the positive component let j = i = +1 in Eq. 4.2, then to first order in $\pi$

$$N^+ = N_0^+ [1 + \sigma_{++}\pi]. \qquad 4.8$$

Insert Eq. 4.6 into 4.8

$$N^+ = N_0^+ [1 - (\sigma_{-0} + \sigma_{0-})\pi]. \qquad 4.9$$

The relative charge fraction follows by dividing Eq. 4.7 by Eq. 4.9

$$\frac{N^-}{N^+} = \sigma_{+-}\pi \left[ \frac{1 - \frac{1}{2}\left(\sigma_{+0} + \sigma_{+-} + \sigma_{-0} + \sigma_{-+} + \frac{\sigma_{+0}\sigma_{0-}}{\sigma_{+-}}\right)\pi}{1 - (\sigma_{+0} + \sigma_{+-})\pi} \right]. \qquad 4.10$$

We now expand the fraction inside the brackets to second order in $\pi$:

$$\frac{N^-}{N^+} = \sigma_{+-}\pi + \frac{1}{2}[\sigma_{+-}(\sigma_{+0} + \sigma_{+-} - \sigma_{-0} - \sigma_{-+}) + \sigma_{+0}\sigma_{0-}]\pi^2. \qquad 4.11$$

The series solution will converge if the following expression holds:

$$\pi(\sum_{i,j} \sigma_{ij}) << 1. \qquad 4.12$$

In our case the largest cross sections involved are thought to be in the range $10^{-15}$ to $10^{-16}$ $cm^2$. Our data would then have to be taken for target thicknesses below $10^{14}$ atoms/$cm^2$.

In this case to a first approximation the above expression would hold and only the linear term in Eq. 4.11 contributes. This is the initial growth in which the charge fraction $N^j/N^i$ is a linear function of pressure. The cross section can be determined by plotting the measured charge fractions for a range of target thicknesses (see Fig. 4.1).

At the upper limits of target thickness secondary processes begin to contribute. From Eq. 4.11 we see that the two step processes would begin to destroy the linearity of the plot at sufficiently high pressures. Because experimental values for these different cross sections were unknown the thin target limit was determined experimentally. The target thickness was kept low enough during measurements that the one step process dominated over the two step while higher order terms could be neglected. Finally a second order least squares fit was done in order to separate the linear from the quadratic term giving the $\sigma_{+-}$ cross section.

### 4.2 Experimental Considerations

In order the measure cross sections the target thickness must be determined. For this the pressure, temperature and target length must be known as accurately as possible.

The target is differentially pumped. At equilibrium, the rate of vapour flow through its apertures is equal to the rate of sublimation, giving a steady state pressure inside the target. The pressure of the magnesium vapour is determined by the coldest region inside the system as long as there are no leaks which would affect the equilibrium. Care was taken in the design of the target apertures so that the gas flow through them was negligible compared to that between the reservoir and target. Vapour pressures were obtained from vapour pressure data published by Hultgren et al.[8]. An overall error of 20%

Fig. 4.1 Quadratic Fit

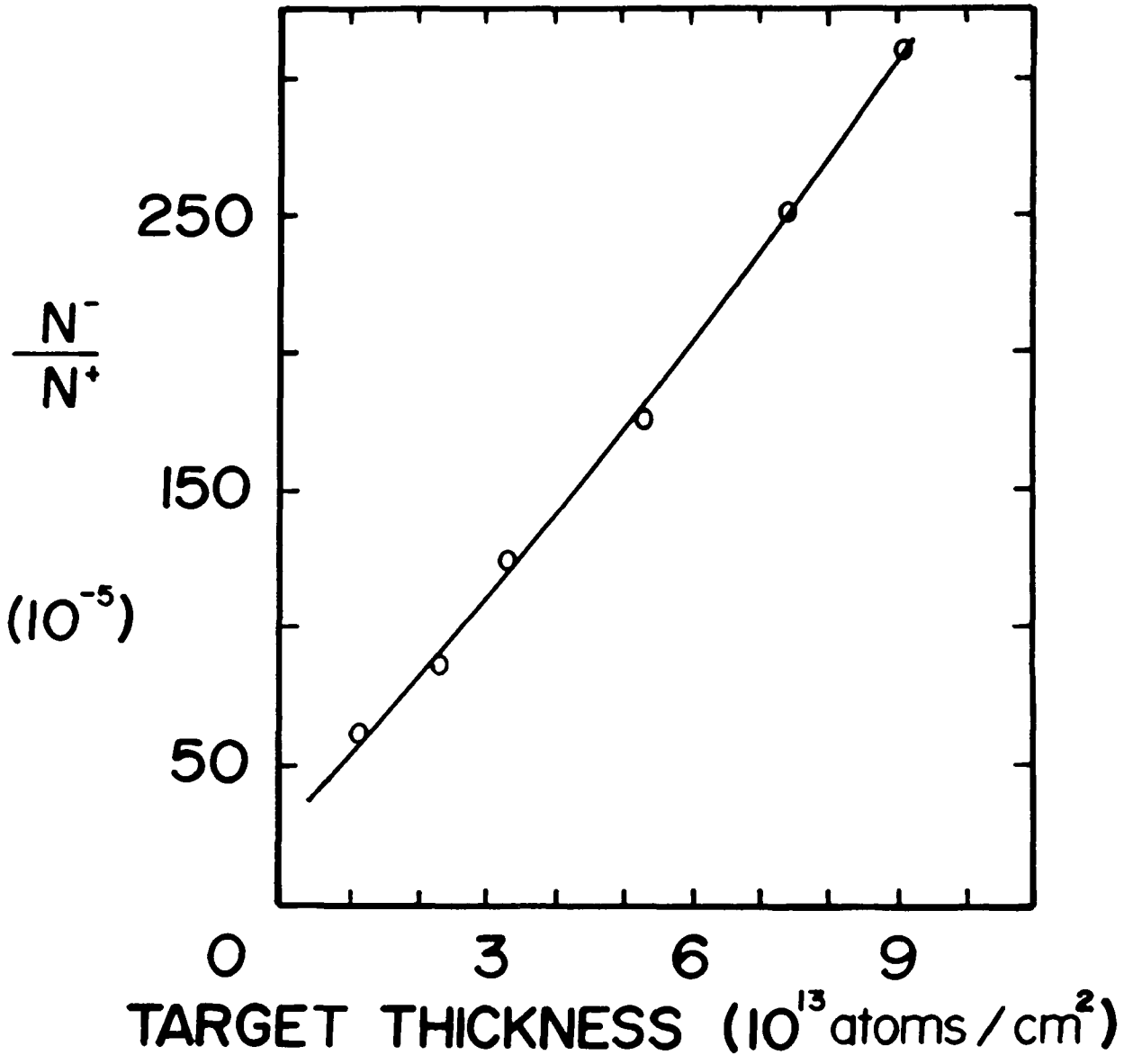

is assessed to the magnitude of the pressure due to the uncertainty of this temperature-pressure conversion. This shows the difficulty of measuring pressure in this manner but still permits a good estimate of the order of magnitude of cross sections. Magnesium vapour would damage conventional pressure sensitive devices.

The modified target geometry was used in which the reservoir was bolted directly to the target. Thermocouples were placed in holes which probed near the magnesium surface; this was assumed to be the coldest region of magnesium exposed to the target in that the reservoir had only one open ended radiation shield surrounding it and was heated entirely by downward conduction from the target. A 30° temperature difference was measured between target and reservoir but a time lag between the negative ion current and reservoir temperature indicated a difference in vapour temperature from that measured; this was thought to be due to poor thermal contact between probe and reservoir and possibly a small temperature gradient existed between the probe and the magnesium surface. To remedy the problem, a calibrated thermocouple was connected directly to the inside of the reservoir at the surface of the magnesium. The thermocouple was calibrated at the National Research Council[9] and was used to calibrate the secondary probes. The calibration was reproducible within 1°C.

In order to obtain a stable magnesium vapour, the powder must be thermally shocked to break oxide layers covering magnesium granules. This was accomplished by keeping the reservoir at high temperature for several hours. Greenbank and Argent[10] found that oxide layers continually reformed as the target outgassed, supressing sublimation and causing pressure oscillations. With our geometry the target could be completely outgassed without

depleting reserves while a titanium getter, which covered most of the interior of the cell, removed oxides before new layers were formed.

As the magnesium vapour began to sublime it was found that it condensed just below the surface, forming a crust and sealing off the lower part of the reservoir. This was verified by inserting a titanium disc at the level of the crust, mechanically sealing off the lower part of the reservoir. Both cases yielded the same results. After several days of running, the upper layer was exhausted and only an oxide shell remained, covering the complete surface and yields began to decrease. In order to prolong the life of the reservoir, cubes cut from magnesium ribbon were placed on top of the powder. This prolonged the life of the reservoir an additional five days.

Measuring cross sections also demands exact target geometry. Entrance and exit tubes were replaced by slits to better define the target length. A three slit system was used where two slits 1 mm internal diameter and 5.3 cm apart aligned the beam entering the target in such a way that it could not strike a 2.2 mm exit slit on the way out (see Fig. 3.1). This insured pressure independance of any slit scattering background signal.

### 4.3 Measurement Procedure

Once the iodine beam was established at each of the energies between 20 keV and 90 keV, the extraction, steering and magnet settings were recorded so that each beam could be reproduced rapidly. The steering settings did not vary greatly so that they could be left at common values for all energies. The extraction voltages increased with energy as expected however, and were adjusted for each energy. Magnet settings were chosen so that they corresponded to the middle of the detection plateau at each energy (see Fig. 2.6). Ion source settings were chosen to give maximum beam current and stability over long periods of time.

The first step was to establish the thin target limit for each energy. This was done by taking a set of measurements over a given range of target thicknesses, then doing the quadratic fit to determine the relative size of the first and second order terms. This process was repeated for smaller and smaller ranges until the two step process was reduced enough that the linear term could be accurately separated out. The thin target limit for most energies was found to be about $10^{14}$ atoms/cm$^2$ as predicted. Once the thin target limit was established measurements were restricted to this region.

To assure stable magnesium vapour pressures the target was heated to a 390°C reference point where the negative component was 1.3% of the positive component at 50 keV. This check was done prior to the measurements and after the measurements were completed.

After the stable target pressure was confirmed, relative charged beam currents were measured at 6 or 7 target thicknesses between $10^{13}$ and $10^{14}$ atoms/cm$^2$. The target was

first stabilized at the highest temperature around 380°C. Measurements were taken for all energies at this point at the same stable temperature within 1°C. The temperature of the target was then decreased by an appropriate amount and the cycle repeated. This procedure was continued until the negative current became too small for an accurate measurement.

After all measurements were completed the relative charged fractions $N^-/N^+$ at each target thickness and energy were tabulated and stored on diskette (see table 4.1). The data was then run in a second order least squares fit program at each energy (In Fig. 4.1 the line represents the fitted curve). From the fit the linear and quadratic terms were evaluated. In the 50 keV to 90 keV range the contribution of the two step process was limited to a maximum of 16% at the highest target thickness (see table 4.2). This gave a good estimate of the magnitudes and energy dependance of the double electron capture cross sections in this range. The cross section peaked between 60 keV and 70 keV (see Fig. 4.2). Below 40 keV the two step process was found to increase and mask the linear term. Measurements for the three lower energies were repeated for 6 or 7 target thicknesses in a lower range in an attempt to reduce the contribution of the two step process. Due to limitations on beam currents at these lower energies the contribution of the two step process could only be reduced to 30% but still permitted the $\sigma_{+-}$ cross section to be evaluated. The cross section decreased in this energy range giving a minimum around 40 keV.

The higher contribution of the two step process increases the uncertainty in the one step cross section. For this reason error bars are included on the graph which denotes the maximum influence of the second order term. The circles represent the $\sigma_{+-}$ cross

Fig. 4.2 Cross Sections

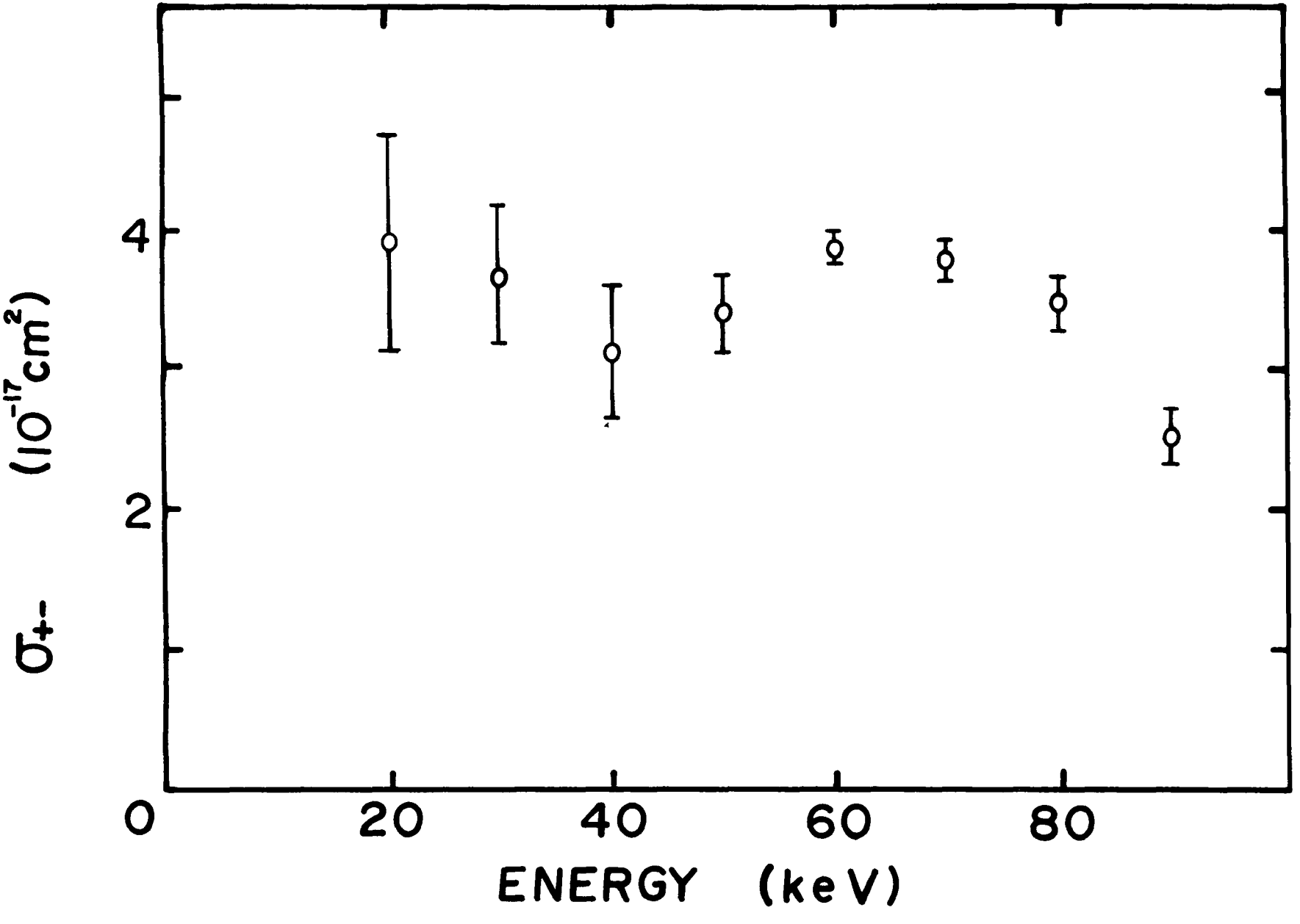

section calculated from the second order fit while the maximum, at the limit of the error, represents the value calculated neglecting the two step process and fitting with a linear relation only. In Table 4.2 the relative contribution of the first and second order terms at maximum target thickness are summarized, including a zero intercept background. The background was found to increase with energy ranging from 0 at low energies to 10% at the maximum energy. The error bars give an estimate of the maximum relative error of the cross sections. A systematic error on the magnitude of these cross sections must also be included due to temperature uncertainty (1%), detection efficiency (3%), along with an overall error on the temperature-vapour pressure calibration of 20%.

**Table 4.1**
*$\sigma_{+-}$ cross section data.*

| Energy (keV) | $\pi$ ($10^{13}$atoms/cm$^2$) | $N^+$ ($10^{-8}$Amps) | $N^-$ ($10^{-11}$Amps) | $N^-/N^+$ ($10^{-5}$) |
|---|---|---|---|---|
| 20 | 1.54 | 0.44 | 0.27 | 61 |
| | 3.33 | 0.42 | 0.69 | 150 |
| | 4.86 | 0.40 | 0.96 | 240 |
| | 5.68 | 0.51 | 1.50 | 294 |
| | 6.81 | 0.60 | 2.30 | 390 |
| | 8.40 | 0.60 | 3.00 | 496 |
| 30 | 1.54 | 1.14 | 0.69 | 60 |
| | 3.33 | 1.50 | 1.90 | 129 |
| | 4.86 | 1.38 | 2.90 | 211 |
| | 5.68 | 1.95 | 5.00 | 256 |
| | 6.81 | 1.35 | 4.50 | 333 |
| | 8.40 | 1.90 | 7.80 | 413 |
| 40 | 1.54 | 1.44 | 0.81 | 56 |
| | 3.33 | 1.35 | 1.70 | 124 |
| | 4.86 | 1.80 | 3.40 | 189 |
| | 5.68 | 2.49 | 5.80 | 235 |
| | 6.81 | 1.50 | 4.60 | 307 |
| | 8.40 | 2.10 | 8.00 | 382 |
| 50 | 1.13 | 0.41 | 0.20 | 45 |
| | 2.30 | 0.37 | 0.36 | 97 |
| | 3.33 | 0.38 | 0.48 | 123 |
| | 5.27 | 0.34 | 0.69 | 205 |
| | 7.42 | 0.36 | 1.08 | 300 |
| | 9.11 | 0.36 | 1.40 | 372 |
| 60 | 1.13 | 0.51 | 0.28 | 52 |
| | 2.30 | 0.49 | 0.47 | 96 |
| | 3.33 | 0.43 | 0.64 | 148 |
| | 5.27 | 0.46 | 0.93 | 207 |
| | 7.42 | 0.47 | 1.38 | 300 |
| | 9.11 | 0.44 | 1.60 | 361 |

**Table 4.1, continued**

| Energy (keV) | $\pi$ ($10^{13}$atoms/cm$^2$) | $N^+$ ($10^{-8}$Amps) | $N^-$ ($10^{-11}$Amps) | $N^-/N^+$ ($10^{-5}$) |
|---|---|---|---|---|
| 70 | 1.13 | 0.54 | 0.32 | 56 |
| | 2.30 | 0.50 | 0.50 | 98 |
| | 3.33 | 0.43 | 0.66 | 150 |
| | 5.27 | 0.47 | 0.96 | 206 |
| | 7.42 | 0.44 | 1.38 | 313 |
| | 9.11 | 0.44 | 1.70 | 380 |
| 80 | 1.13 | 0.62 | 0.39 | 62 |
| | 2.30 | 0.43 | 0.54 | 126 |
| | 3.33 | 0.61 | 0.78 | 130 |
| | 5.27 | 0.57 | 1.14 | 201 |
| | 7.42 | 0.48 | 1.44 | 300 |
| | 9.11 | 0.54 | 2.00 | 365 |
| 90 | 1.13 | 0.87 | 0.51 | 59 |
| | 2.30 | 0.92 | 0.78 | 85 |
| | 3.33 | 0.84 | 1.02 | 124 |
| | 5.27 | 0.90 | 1.56 | 175 |
| | 7.42 | 0.83 | 2.00 | 251 |
| | 9.11 | 0.78 | 2.40 | 308 |

**Table 4.2**

*Relative magnitudes of the 0, $1^{st}$ and $2^{nd}$ order terms at maximum target thickness.*

| Energy (keV) | 20 | 30 | 40 | 50 | 60 | 70 | 80 | 90 |
|---|---|---|---|---|---|---|---|---|
| $\sigma_{+-}$ ($10^{-17}cm^2$) | 3.9 | 3.7 | 3.1 | 3.4 | 3.9 | 3.8 | 3.3 | 2.5 |
| $1/2\Sigma\sigma_{ij}\sigma_{ji}$ ($10^{-32}cm^4$) | 25 | 16 | 17 | 7 | 1 | 3 | 5 | 6 |
| $1^{st}$order (%) | 65 | 74 | 68 | 84 | 96 | 90 | 83 | 75 |
| $2^{nd}$order (%) | 35 | 26 | 31 | 14 | 3 | 7 | 11 | 16 |
| 0 order (%) | - | - | 1 | 2 | 1 | 3 | 6 | 9 |

## CHAPTER 5-*Summary and Discussion of Results*

The Danfysik 911A ion source was found to produce intense and stable ion beams for elements with wide ranging vapour pressures. The intensities were high enough that useful negative ion beams could be produced even if only a small percentage of ions were converted in a charge changing cell. The stability of the arc discharge method would prove advantageous over the R.F. method, particularly when using beams for diagnostics where beam fluctuations limit resolution.

The target design proved to be very versatile and efficient for negative ion production. The heating method and temperature measurement and stabilization were found to be very dependable. Heaters and temperature probes worked without failure for over one year. One drawback was discovered when using magnesium in the reservoir: oxide husks which were left behind after the magnesium had sublimed began to build up and cover the remaining reserves causing the conversion efficiency to decrease. A proposed modification to the reservoir would allow these husks to fall between the magnesium cubes. This proposed change would also allow the use of a reservoir which included the thermocouple probe on the inside; this would then increase the accuracy of the temperature measurement.

Negative ion yields were found to reach a maximum at target thicknesses of the order of $10^{15}$ atoms/cm$^2$ (440°C). At this point the negative and positive yields were about equal. This crossing of the negative and positive yield curves (see Fig. 3.6) occurs at similar target thicknesses to those found by Hvelplund et al.[1] for projectiles with similar electron affinities. The negative yield dominates at our highest target thickness as expected due to the high electron affinity of iodine. The reason that the projectiles with high electron

affinities give higher negative yields in magnesium than in sodium, despite the latter's lower ionization potential, may be related to the fact that even though the $\sigma_{0-}$ cross-section favours targets with low ionization potentials, the $\sigma_{+0}$ cross section favours targets with higher ionization potentials. For projectiles with high electron affinities the $\sigma_{+0}$ cross section seems to become the more dominant of the two. These two cross sections are thought to have the most influence on the relative size of the equilibrium fractions.

From Fig. 3.5 we saw that the negative current reached a maximum at a target thickness of about $150 \times 10^{13}$ atoms/cm$^2$. Even though the negative yield was still rising at this point, the overall current began to decrease. This was due to the size of the exit aperture and the scattering of the ions in multiple target collisions. At this maximum the negative ion current was about 25% of the current entering the target, which would give ample charge conversion for most applications. The beam was well collimated as it emerged from the target: the exit aperture was $\frac{1}{16}$" in diameter and $1\frac{1}{2}$" long. Ions scattered at angles larger than about $2^\circ$ would not exit the canal without striking the tube and would not contribute to the peak obtained in our experiments. On the other hand, if the beam profile were not critical for a particular measurement, the exit tube diameter could be increased to obtain more beam, without affecting the beamline or the target pressures.

The double electron capture process was found to be too small to contribute greatly to the equilibrium yields. The double electron capture cross section decreased from about $4 \times 10^{-17}$cm$^2$ at 20 keV down to about $2.5 \times 10^{-17}$ cm$^2$ at 90 keV. A minimum and subsequent maximum in cross section was found to occur between these two energies. The extent of this structure was difficult to resolve however, due to the relative errors assessed

to these measurements. These errors were due to the second order term in the quadratic fit which decreases the accuracy of the measurement of the linear term. The second order term, which originates mainly from two successive single electron captures, was found to be much larger at the lower energies. The magnitude of this second order term at 20 keV, which determines $\sigma_{+0}\sigma_{0-}$ to a first approximation, confirmed the success of the second order fit. This factor had the same order of magnitude as that calculated from the single detachment cross sections estimated by Hvelplund et al.[1]. At higher energies the correction decreased and the decrease in the $\sigma_{+-}$ cross section, from 60 to 90 keV, is definite.

A negative background current which increased with energy was found on all our results above 30 keV. This background, which was also observed in the data of Morgan et al.[11], was attributed by us to slit scattering of the ions as they entered the target. This negative component, which is unlikely to be caused by any other process, was unexpected in that positive ions are not known to have a negative reflection component when scattered from metal surfaces.

The overall energy dependance of the double electron capture cross section is similar to that obtained by Morgan et al. for protons incident in a magnesium vapour. The structure in their results was attributed to transitions at two different energy level crossings in the $(HMg)^+$ quasi-molecular structure. The $(IMg)^+$ system is expected to have similar structure but the overall maximum in the cross section would be expected at lower projectile velocities due to the energy defects involved. As a general rule the maximum in the cross section is found at higher projectile velocities for processes with higher energy defects. Table 5.1 summarizes the only known data on the double electron capture process.

**Table 5.1**

*Existing data on double electron capture (including the single electron capture of I on Mg).* $|\Delta E| = |\Delta E_\infty - \Delta E_c|$

| Collision | Process | Cross section $(10^{-17} cm^2)$ | $v_{max}$ $(10^7 m/s)$ | $\Delta E_\infty$ (eV) | $E_c$ (eV) | $\lvert\Delta E\rvert$ (eV) |
|---|---|---|---|---|---|---|
| $I^+ \rightarrow Mg^1$ | $\sigma_{0-}$ | 100 | 1 | 4.58 | 5.88 | 1.30 |
| $I^+ \rightarrow Mg$ | $\sigma_{+-}$ | 3.8 | 3 | 9.12 | 11.76 | 2.64 |
| $C^+ \rightarrow Xe^{12}$ | $\sigma_{+-}$ | 6.0 | 9 | 20.86 | 12.82 | 8.04 |
| $H^+ \rightarrow Mg^{11}$ | $\sigma_{+-}$ | 3.5 | 10 | 8.33 | 22.47 | 14.14 |

From this data we see a definite increase in $v_{max}$ with energy defect. The maximum obtained in our measurements fits in with the the existing data and therefore explains the decrease in cross section at higher energies. The relative magnitudes of these cross sections do not follow the classical theory however. As discussed in the introduction the cross sections should in general increase with decreasing energy defects. In comparing our results with that of Fogel et al.[12], the classical results are not observed. Fogel et al. found a cross section of $6 \times 10^{-17}$ cm$^2$ for carbon ions incident on a xenon target where the energy defect is 8.04 eV. The structure of the magnesium atom should favour double electron transfer in that it has two loosely bound electrons. The energy defect is reduced to 2.64 eV when taking into account the coulomb energy; this is much smaller than that of the $C^+ \rightarrow Xe$ collision although the cross section is found to be much smaller. This result is unexplained by the classical theory. Dubois et al.[13] also found irregularities with cross sections involving the magnesium target when comparing the single and double electron capture cross sections of H and He ions in Mg and Na targets. For the single detachment the Na target gives larger cross sections as expected from the classical theory, but double electron capture is predicted to be larger in Mg than in Na, the opposite of what is observed.

This phenomena may be partly explained however by recent calculations of Krause et al.[14] who found evidence that the two electrons in the outer shell of the magnesium atom may be strongly correlated to be on opposite sides of the atom and therefore may not both be seen by an oncoming fast projectile. Further work is needed to take these interactions into account in multiple electron transfer calculations.

## REFERENCES


1. J. Heinemeier and P. Hvelplund, Nucl. Instr. Meth. 148, 65(1978).

2. B. Hird, C. Pepin and G. Kelly, J. Appl. Phys. 56, 3304(1984).

3. S. K. Allison, Rev. Mod. Phys. 30, 1137(1958).

4. J. Heinemeier and P. Tykesson, Rev. Physique Appliquee 12, 1471(1977).

5. J. Heinemeier and P. Hvelplund, Nucl. Instr. Meth. 148, 425(1978).

6. Kenward, Kinetic Theory of Gases, 302(1938), McGraw-Hill.

7. V.S. Nicholaev, I.S. Dmitriev, L.N. Fateeva and Ya.A. Teplova, Zh. Eksp. Teor. Fiz. 40, 989 (1961) [Sov. Phys. -JETP 13, 695 (1961)].

8. R. Hulgren, P.D. Desai, D.T. Hawkins, M. Gleiser, K.K. Kelley, and D. Wagman, Selected Values of the Thermodynamic Properties of the Elements (American Society of Metals, Metals Park, Ohio, 1973).

9. Calibration performed by D. Lawer of the Physics Division, National Research Council, Ottawa.

10. J.C. Greenbank and B.B. Argent, Trans. Faraday Soc. London, 61, 655(1965).

11. T.J. Morgan and F.J. Eriksen, Phys. Rev. 19, 1448(1979)

12. Ia.M. Fogel', R.V. Mitin and A.G. Koval', Zh. Eksp. Teor. Fiz. 31, 397 (1956), [Sov. Phys. JETP 4, 359 (1957)].

13. R.D. Dubois and L.H. Toburen, Phys. Rev. A31, 3603(1985).

14. J.L. Krause and R.S. Berry, Phys. Rev. A31, 3502(1985).